

View Article Online **PAPER**



Cite this: Phys. Chem. Chem. Phys., 2023, 25, 11986

Received 28th February 2023,

Accepted 6th April 2023 DOI: 10.1039/d3cp00936i

rsc.li/pccp

Absolute quantum yield for understanding upconversion and downshift luminescence in PbF₂:Er³⁺,Yb³⁺ crystals†

Eduard Madirov, Da Dmitry Busko, Da lan A. Howard, Dab Bryce S. Richards Dab and Andrey Turshatov **

The search for new materials capable of efficient upconversion continues to attract attention. In this work, a comprehensive study of the upconversion luminescence in PbF₂:Er³⁺,Yb³⁺ crystals with different concentrations of Yb3+ ions in the range of 2 to 7.5 mol% (Er3+ concentration was fixed at 2 mol%) was carried out. The highest value of upconversion quantum yield (ϕ_{UC}) 5.9% (at 350 W cm⁻²) was found in the PbF₂ crystal doped with 2 mol% Er^{3+} and 3 mol% Yb^{3+} . Since it is not always easy to directly measure ϕ_{UC} and estimate the related key figure of merit parameter, saturated photoluminescence quantum yield (ϕ_{UCsat}), a method to reliably predict ϕ_{UCsat} can be useful. Judd–Ofelt theory provides a convenient way to determine the radiative lifetimes of the excited states of rare-earth ions based on absorption measurements. When the luminescence decay times after direct excitation of a level are also measured, ϕ_{UCsat} for that level can be calculated. This approach is tested on a series of PbF₂:Er³⁺,Yb³⁺ crystals. Good agreement between the estimates obtained as above and the directly experimentally measured ϕ_{UCsat} values is demonstrated. In addition, three methods of Judd-Ofelt calculations on powder samples were tested and the results were compared with Judd-Ofelt calculations on single crystals, which served as the source of the powder samples. Taken together, the results presented in our work for PbF₂:Er³⁺, Yb³⁺ crystals contribute to a better understanding of the UC phenomena and provide a reference data set for the use of UC materials in practical applications.

Introduction

The synthesis of materials with efficient upconversion (UC) luminescence is a hot topic in materials science due to their use in a wide range of applications. These include potential applications in photovoltaics and solar energy harvesting, 1-3 security markers, 4-7 luminescent thermometry, 8,9 as well as tracers for advanced plastics sorting.10 Most of these applications are made possible by the unique optical properties of the trivalent ions of the lanthanides, which are defined by partially forbidden transitions within 4f electronic shells. UC processes in lanthanide doped materials can be realised by excited state absorption, photon avalanche or energy transfer up-conversion (ETU),¹¹ with ETU providing the highest photoluminescence quantum yield (ϕ_{UC}) at intensities that can be regarded as low (<40 W cm⁻²).¹²⁻¹⁴

Recently, efficient ETU in crystalline materials based on MF₂ (M = Ca, Sr, Ba) hosts doped with Er³⁺ and Yb³⁺ has received increasing attention. 15-19 These hosts generally have a cubic unit cell, which is considered unfavourable for radiative transitions and efficient energy transfer between doping ions, which is crucial for the ETU process. However, when doped with trivalent lanthanide ions, the symmetry of the local environment is reduced, increasing the probability of the transitions. This is because trivalent ions replace divalent cations and require charge compensation via F ions taking interstitial positions in the lattice.²⁰⁻²³ In addition, MF₂ hosts tend to have a lower maximum phonon energy than other fluoride hosts: CaF₂ - 320 cm⁻¹, ²⁴ SrF₂ - 284 cm⁻¹, ²⁴ BaF₂ - 240 cm⁻¹ 24 *versus* β-NaYF₄ – 360 cm⁻¹, 25 LaF₃ – 350 cm⁻¹, 26 and LiYF₄ – 460 cm⁻¹.^{27,28} Low phonon energy hosts favour achieving high $\phi_{\rm UC}$ values. For near-infrared (980 nm) to visible UC, the highest ϕ_{UC} values observed in MF $_2$ materials are 6.5% in SrF₂:Er³⁺,Yb³⁺¹⁶ and 10.0% in BaF₂:Er³⁺,Yb³⁺,¹⁹ whereas the highest known ϕ_{UC} in a material doped with $\mathrm{Er^{3+}}$ and $\mathrm{Yb^{3+}}$ ions is 11% in β-NaYF₄.¹³ However, to date, there have been

^a Institute of Microstructure Technology, Karlsruhe Institute of Technology, Hermann-von-Helmholtz-Platz 1, 76344 Eggenstein-Leopoldshafen, Germany. E-mail: andrey.turshatov@kit.edu

^b Light Technology Institute, Karlsruhe Institute of Technology, Engesserstrasse 13, 76131 Karlsruhe, Germany

[†] Electronic supplementary information (ESI) available. See DOI: https://doi.org/ 10.1039/d3cp00936j

only a small number of publications on lanthanide-doped crystalline PbF2 hosts. From the available data it can be inferred that \mbox{PbF}_2 doped with \mbox{Er}^{3^+} and \mbox{Yb}^{3^+} should perform similarly to the other materials mentioned above due to low phonon energy $(257 \text{ cm}^{-1})^{29}$ In addition, the observed ϕ_{UC} increases when moving from SrF2 to BaF2 thus suggesting that heavier cations help to achieve high ϕ_{UC} values, thus PbF $_2$ could offer even better UC performance.

Usually, the UC samples can be obtained either in a form of micro/nanometer size particles or in a form of single crystals. While the characterisation of crystalline materials is best performed when the samples are in the form of single crystals due to the convenient and reliable measurement of the absorption coefficient, luminescence decay time and $\phi_{\rm UC}$ value as well as Judd-Ofelt (JO) calculations, the micro- or nanoparticles are often more feasible for applications and easier to synthesise. Thus, it is crucial to compare the results obtained with these two forms of the material.

This paper presents a comprehensive study of PbF2 crystals doped with Er3+ and Yb3+ - the Er3+ concentration was set to either 2 or 1.5 mol% and the Yb3+ concentration was varied in the range 1.5-7.5 mol%. To gain insight the upconversion properties of the studied crystals, both the power density dependent ϕ_{UC} under 976 nm excitation and the downshifting quantum yield (ϕ_{DS}) under 522 and 652 nm excitation were obtained. The analysis of $\phi_{\rm UC}$ and $\phi_{\rm DS}$ values and radiative lifetimes from JO calculations was used to understand the UC mechanism and to find factors limiting $\phi_{\rm UC}$ in Yb³⁺/Er³⁺ codoped PbF2 crystals. In addition, powder samples prepared by grinding the above crystals were studied. JO analysis on crystalline and powder samples provided a useful comparison of three different methods for calculating JO parameters on powder materials.

Experimental part

Synthesis procedure

The single crystals based on PbF₂ doped with Yb³⁺ and Er³⁺ were grown by the Bridgman technique in a vacuum using the CF₄ fluorination atmosphere in multichannel graphite crucibles with a temperature gradient (7 deg mm⁻¹). The growth rate (7 mm hour⁻¹) was estimated from the stability function of a flat crystallization front.³⁰ Based on the PbF₂-RF₃ (R = Yb, Er)³¹ phase diagrams, the single crystal growth temperature was chosen to be 870 °C. The crystalline samples were prepared in a shape of disks 10 mm in diameter and about 1.7 mm in thickness, cut perpendicular to the long axis of the crystal boule.

Characterization

To estimate maximum host phonon energy, the Raman spectrum of the undoped PbF₂ sample was recorded (Polytec i-Raman instrument) using 785 nm excitation and with a 3.5 cm⁻¹ resolution. It was not possible to obtain the Raman spectrum of a doped PbF₂ sample due to presence of emission from ⁴I_{9/2} energy level of Er³⁺ under 785 nm excitation that makes the detection of the pure Raman bands complicated.

The crystalline structure of the samples was determined using the powder XRD patterns recorded with a diffractometer (Bruker, D2 PHASER) (CuKα radiation). A small part of the single crystal was ground into powder. The patterns were recorded in the 2 theta range from 10 to 70 degrees.

Absorption spectra of the crystals were recorded at a room temperature using a ultraviolet (UV)-visible (Vis)-NIR spectrophotometer (PerkinElmer Lambda 950) in absorbance mode. The instrument provided the absorbance data, which was then converted to the absorption coefficient using eqn (1):

$$\alpha = -\frac{1}{d} \ln(10^A) \tag{1}$$

where α is the absorption coefficient in cm⁻¹, A is the absorbance data obtained from the instrument, and d is sample thickness in centimetres.

The concentration of Er³⁺ and Yb³⁺ ions (Table S2, ESI†) was determined by wavelength dispersive X-ray fluorescence (WDXRF) spectroscopy (Pioneer S4, Bruker AXS).

Excitation spectra were recorded using a calibrated spectrophotometer (Varian Cary Eclipse). Diffuse reflectance spectra were recorded at room temperature using a spectrophotometer (PerkinElmer Lambda 950) in absorbance mode with the sample placed inside an integrating sphere.

The setup and the methodology for estimating ϕ_{UC} under 976 nm excitation have been described previously. 16,19,32 The setup is built around an integrating sphere (Labsphere, Ø6", 3 P-LPM-060-SL) and uses two calibrated spectrometers (Avantes, AvaSpec-ULS2048×64TEC, Thorlabs, CCS200/M) to register the intensity of the sample emission and the incident laser. A 976 nm laser diode (Roithner) driven by a laser diode controller (ITC4001, Thorlabs) is used as the excitation source and the incident intensity is varied with a variable filter wheel (Thorlabs, NDC-100C-2).

To record the $\phi_{\rm DS}$ of the $^4{
m S}_{3/2}$ ightarrow $^4{
m I}_{15/2}$ and $^4{
m F}_{9/2}$ ightarrow $^4{
m I}_{15/2}$ transitions of the Er³⁺ ions, a tunable continuous wave (CW) laser (Solstis with EMM-Vis, M-Squared Lasers Ltd) pumped by 532 nm laser (Verdi-V18, Coherent) is used. The system is tuned to 522 nm for the direct excitation of the ⁴S_{3/2} level and to 652 nm for the direct excitation of the ⁴F_{9/2} level. For the measurement of $\phi_{\rm DS}$ of the ${}^4{\rm I}_{13/2} \rightarrow {}^4{\rm I}_{15/2}$ transition under direct excitation the tunable laser kit (Thorlabs, TLK-L1550M) operating at 1495 nm was used as the excitation source. The rest of the setup was the same as described in our previous publication. 19,32

Luminescence lifetimes are measured using an optical system described previously. 17,19 525 nm, 976 nm, and 633 nm (Roithner) and 1550 nm (Thorlabs) laser diodes mounted in temperature stabilized mounts (TCLDM9, Thorlabs) and driven by a laser diode controller (ITC4001, Thorlabs) are used as the excitation sources. The luminescence wavelength is selected with a double monochromator (Bentham, DTMS300) and the signal is detected with a photomultiplier tube (R928P, Hamamatsu) mounted in a temperature-cooled housing

(CoolOne, Horiba) in the UV-Vis region or with an infrared single-photon detector (ID Quantique, ID220) in IR region-both detectors are coupled to the multi-channel scaling card (Time-Harp 260, Picoquant).

Results and discussion

Crystal structure characterization

The measured powder XRD patterns are presented in Fig. 1(a). The data is in good agreement with JCPDS card # 76-1816. The XRD patterns show that the parameters of a unit cell change with doping concentration. To illustrate this the position of the [111] peak in samples with different Yb³⁺ contents is plotted in Fig. 1(b). The position of the [111] peak is shifted to the higher angles as the concentration of the dopant ions is increased. This is due to the fact that the ionic radius of the Er³⁺ and Yb³⁺ ions is smaller than that of the Pb2+ ions, which causes the shrinking of the unit cell in samples with higher doping concentration. The Raman spectrum for an undoped PbF2 crystal is presented in Fig. 1(c). It consists of a broad band with a maximum at 260 cm⁻¹. This value agrees well with the previously reported phonon energy of a PbF₂ crystal equal to 257 cm⁻¹.²⁹

Absorption spectra and JO calculations

The absorption spectra of the samples investigated are given in Fig. 2. The spectra contain absorption bands in the UV, Vis and NIR regions typical for Er³⁺ and Yb³⁺ ions. The transitions corresponding to the most intense bands are labelled in Fig. 2. The positions of all bands remain the same in all samples and

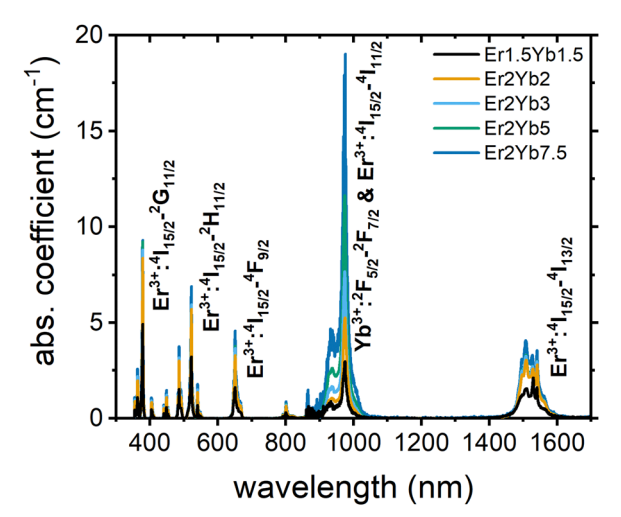


Fig. 2 Absorption spectra of the PbF₂:Er³⁺,Yb³⁺ crystals.

are in agreement with the available literature data. 16,19 The absorption data can be used in the JO method to calculate key features of electron levels in luminescent materials, such as radiative lifetime and branching ratios. The comparison of these radiative lifetimes with experimentally obtained luminescence decays can additionally reveal the fraction of excitation energy emitted via radiative processes, which, in turn, can help to predict both the down-shifting quantum yield ϕ_{DS} and the upconversion quantum yield ϕ_{UC} . 33,34

A standard procedure was used to obtain JO parameters in our work. 35,36 The IO theory uses absorption cross-sections to determine oscillator strengths (Table S1, ESI†). These values were then used to calculate JO parameters Ω_t , which allow the

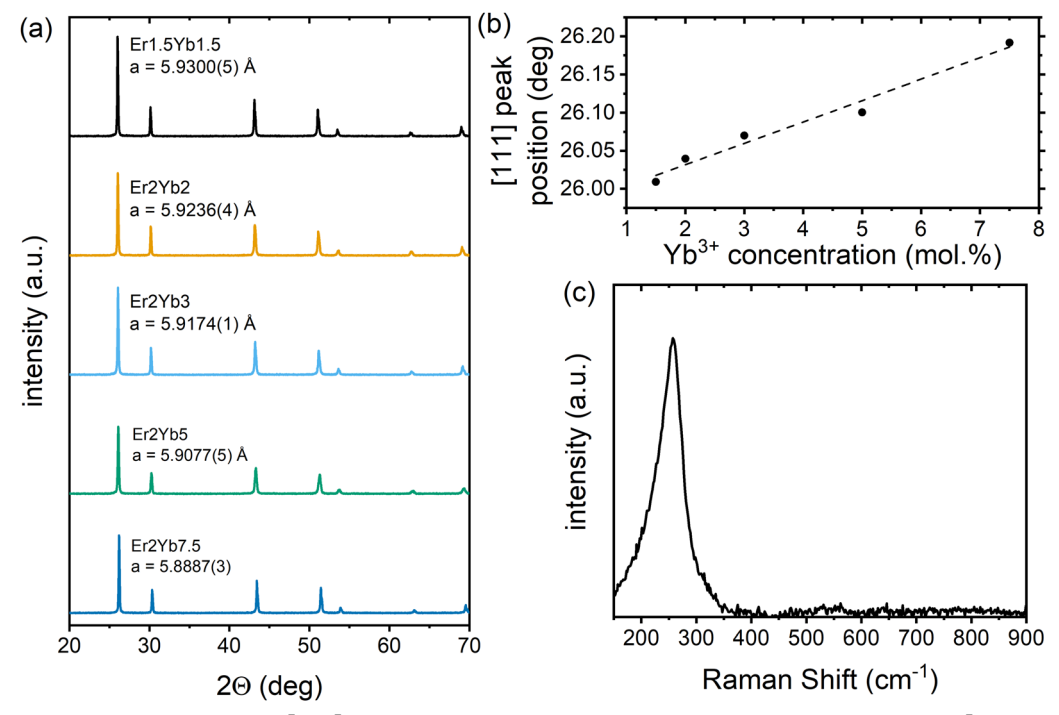


Fig. 1 (a) Powder XRD patterns of the PbF₂:Er³⁺,Yb³⁺ samples; (b) change in the [111] peak position with increasing Yb³⁺ concentration; (c) room temperature Raman spectrum of the undoped PbF2 crystal.

Table 1 Barycentre wavelength (λ_b) , along with literature values for the reduced matrix elements $(U)^{37}$ and refractive index $(n)^{38}$ of the host at the appropriate wavelengths

Excited state	$\lambda_{\rm b}$, nm	$[\mathit{U}^{(2)}]$	$[\mathit{U}^{(4)}]$	$[U^{(6)}]$	n
$^{4}G_{11/2}$	378.5	0.9156	0.5263	0.1167	1.8314
$^{2}H_{9/2}$	406.5	0	0.0243	0.2147	1.8149
$^{4}F_{7/2}$	487.0	0	0.1465	0.6272	1.7857
$^{2}H_{11/2}$	522.0	0.7158	0.4128	0.0927	1.7774
$^{4}S_{3/2}$	542.0	0	0	0.2235	1.7740
$^{4}F_{9/2}$	653.0	0	0.55	0.4621	1.7593
$^{4}I_{13/2}$	1520.0	0.0195	0.1172	14.325	1.7335

description of a radiative transition between any two levels. To obtain the $\Omega_{\rm t}$ values, some additional parameters, such as the barycentre wavelength, the doping concentration of ${\rm Er}^{3+}$ ions, the refractive index and the reduced matrix elements should be accurately estimated beforehand. These values are given in Table 1 (reduced matrix elements 37 and refractive index data 38 were taken from the literature and are universal for all samples) and Table S2, ESI† (concentrations of doping ions estimated by the WDXRF method).

Briefly, the parameters used in the JO calculations are obtained as follows. The absorption cross sections were calculated from the absorption spectra shown in Fig. 2 and the doping concentration of the Er^{3+} ions. The barycentre energy

 $(E_{\rm b})$ and then the barycentre wavelength $\left(\lambda_{\rm b} = \frac{h \cdot c}{E_{\rm b}}\right)$ were determined using the method described by Hehlen et al.35 In general, when an absorption band spans over energies from E_0 to E_1 then E_b is defined as $\int_{E_0}^{E_b} \alpha(\lambda) d\lambda = \int_{E_b}^{E_1} \alpha(\lambda) d\lambda$ where $\alpha(\lambda)$ is absorption cross-section. The reduced matrix elements are taken from the work of Carnall et al.37 as Hehlen et al.35 demonstrated that the host has an insignificant effect on the values of the reduced matrix elements. The refractive indices nof the PbF₂ corresponding to the wavelength of each absorption transition in the Er³⁺ ions are taken from the work of Malitson and Dodge.³⁸ The root mean square (RMS) approach described by Hehlen et al. 35 was used to calculate the JO parameters Ω_t . This approach allows to reduce the influence of more intense absorption bands on the calculation result. The uncertainties in the JO parameters Ω_t were calculated using the matrix approach described by Zhang et al.39 and by Görller-Walrand and Binnemans.40 The uncertainty of the radiative lifetime

could also be calculated from the known uncertainty in $\Omega_{\rm t}$ (Table 2). The full results of the JO calculations are given in the Tables S2–S7 (ESI†), while Table 2 summarizes the values of radiative lifetimes ($\tau_{\rm rad}$) and branching ratios (β) that are important for the further discussion.

The following observations can be made from these results. Firstly, the increase in the doping concentration of Yb³⁺ leads to higher transition probabilities in Er³⁺ and thus shorter Er³⁺ radiative times. On the other hand, the branching ratios are similar in all samples. Unfortunately, in many cases there is no a simple relationship between the radiative lifetime and the number of emitted photons emitted, since non-radiative relaxation and various quenching processes must be taken into account. Nevertheless, the study of luminescence decay and knowledge of the radiative lifetime is a useful data set that can shed light on the quantum yield of luminescent materials.

Fig. 3(a) demonstrates the luminescence spectra of the PbF₂:Er³⁺,Yb³⁺ crystals excited at a wavelength of 375 nm. The emission spectra consist of several peaks corresponding to ${}^{4}S_{3/2} - {}^{4}I_{15/2}, {}^{4}F_{1/2} - {}^{4}I_{15/2}, {}^{4}S_{3/2} - {}^{4}I_{13/2}, {}^{4}Er^{3+} : {}^{4}I_{11/2} & Yb^{3+} : {}^{2}F_{7/2} - {}^{4}F_{11/2} - {}$ ${}^{4}I_{15/2}$ and ${}^{4}I_{13/2}$ $-{}^{4}I_{15/2}$ transitions. In order to correlate the results of the JO calculations with the experimental results, the luminescence decays of three states (${}^4S_{3/2}$, ${}^4F_{1/2}$ and ${}^4I_{13/2}$) were studied (Fig. 3(b)-(d)) using the direct excitation of the above states. The first interesting observation based on these decays is that the decay time of the 4I13/2-4I15/2 transition (Fig. 3(d) and Table S8, ESI†) is always longer than the radiative lifetime calculated using the IO model (Table 2). The uncertainties of the experimentally determined decay times were calculated using a method described in the work of Fišerová and Kubala.41 It can be assumed that such an extension of the decay time is due to the re-absorption of emitted photons within the crystal. 42,43 To test this hypothesis, two exemplary crystals (Er2Yb5 and Er2Yb2) were carefully ground and the powder was diluted with undoped PbF2 powder (the experimental protocol is inspired by the works of de Mello Donegá et al. 42 and Rabouw et al. 43) until the ratio between the undoped and doped fractions was 19 to 1. In such an experiment, the local concentration of Er3+ and Yb3+ remains unchanged, whereas the reabsorption can be significantly reduced by dilution. Indeed, the dilution led to a pronounced reduction in the decay time (Fig. 3(e)), which decreased from 8.8 ms to 5.4 ms for the powder with undoped/doped (Er2Yb5 crystal) ratios of

Table 2 Radiative lifetimes (τ_{rad}) and branching ratios (β) of some transitions of the PbF₂:Er³⁺,Yb³⁺ samples, and calculated Judd-Ofelt parameters

		Er1.5Yb15	Er2Yb2	Er2Yb3	Er2Yb5	Er2Yb7.5
$^{4}S_{3/2}$ $^{-4}I_{15/2}$	$\tau_{\rm rad}$, ms β	1.12 ± 0.06 0.67	0.85 ± 0.05 0.67	0.81 ± 0.04 0.67	0.82 ± 0.04 0.67	0.63 ± 0.04 0.67
$^4\mathrm{F}_{9/2} - ^4\mathrm{I}_{15/2}$	$\tau_{\rm rad}$, ms	1.47 ± 0.14 0.91	$1.11 \pm 0.12 \\ 0.91$	1.06 ± 0.09 0.91	1.03 ± 0.11 0.91	0.86 ± 0.10 0.92
$^{4}I_{13/2}$ $-^{4}I_{15/2}$	$\tau_{\rm rad}$, ms β	9.71 ± 0.17 1.00	8.39 ± 0.20 1.00	8.12 ± 0.17 1.00	8.17 ± 0.19 1.00	7.00 ± 0.21 1.00
Judd-Ofelt para	meters, ×10 ⁻²⁰ c	em²				
Ω_2		1.053 ± 0.105	1.342 ± 0.134	0.986 ± 0.099	0.952 ± 0.095	1.289 ± 0.129
$rac{\Omega_4}{\Omega_6}$		$egin{array}{l} 0.836 \pm 0.125 \ 0.839 \pm 0.042 \end{array}$	$egin{array}{l} 0.469 \pm 0.070 \ 1.795 \pm 0.090 \end{array}$	$egin{array}{l} 1.163 \pm 0.174 \ 1.160 \pm 0.058 \end{array}$	$egin{array}{l} 0.125 \pm 0.019 \ 1.140 \pm 0.057 \end{array}$	$\begin{array}{c} \textbf{1.381} \pm \textbf{0.207} \\ \textbf{1.480} \pm \textbf{0.074} \end{array}$

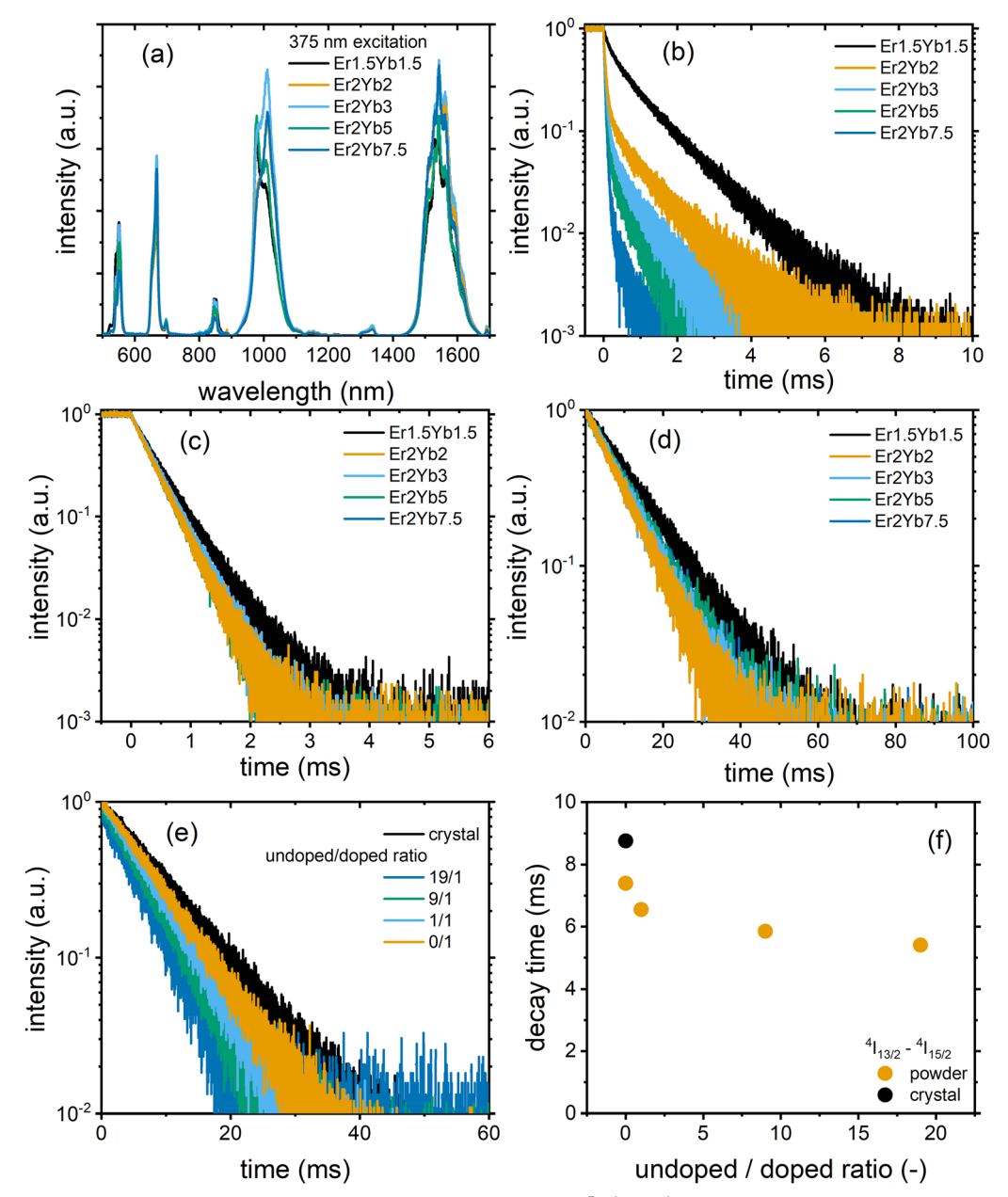


Fig. 3 (a) Emission spectra under 375 nm excitation, (b) luminescence decay of the Er^{3+} : ${}^4S_{3/2} - {}^4I_{15/2}$ transition under 525 nm excitation, (c) luminescence decay of the Er^{3+} : ${}^4I_{15/2} + {}^4I_{15/2} +$ the PbF₂: Er³⁺, Yb³⁺ samples; (e) luminescence decay and (f) luminescence decay time of the Er³⁺.4 $I_{13/2}$ of the PbF₂:2 mol% Er³⁺,5 mol% Yb³⁺ crystal and diluted powders under 1535 nm excitation.

9/1 and 19/1 (Fig. 3(f)). The luminescence decays of the other two transitions ${}^4S_{3/2} - {}^4I_{15/2}$ and ${}^4F_{9/2} - {}^4I_{15/2}$ were also prolonged in the crystal (which may indicate an effect of re-absorption), but to a much lesser extent (Fig. S1, ESI†). Another example of data with a similar trend can be found in ESI† for the crystal Er2Yb2 (Fig. S2, ESI†).

A second interesting phenomenon can be observed in Fig. 3(b) with multi-exponential behaviour of all decays. It is well known that the 4S_{3/2} state of Er³⁺ undergoes cross-relaxation with the ground states of $\mathrm{Er^{3+}(^4I_{15/2})}$ and $\mathrm{Yb^{3+}(^2F_{5/2}).^{44}}$ Due to the distribution of the inter-ion distance (Er3+-Er3+ or Er3+-Yb3+) the cross-relaxation rate can take different values, resulting in a multi-exponential decay. For simplicity, the decays in Fig. 3(b) were fitted with a bi-exponential model, giving the results shown in Table S8 (ESI†). It is important to note that crystals with the lowest Er3+ concentration (Er1.5Yb1.5 and Er2Yb2) demonstrate the presence of the short-lived component with decay times of 0.18 and 0.08 ms and a significant contribution from the long-lived component with decay times of 1.08 and 0.94 ms, respectively. Simultaneously, the JO calculation predicts radiative lifetimes of 1.12 and 0.85 ms (Table 2), respectively. Thus, the close examination of the decays for Er1.5Yb1.5 and Er2Yb2 crystals

shows that the long-lived component of the decay is close to or even exceeds the radiative lifetime obtained with the IO method, which cannot be explained by simple re-absorption (with almost no extension of the experimental decay times in Fig. S1 and S2, ESI†) and requires a reasonable explanation.

It can be assumed that due to the formation of clusters of lanthanide ions in MF2 (M = Ca, Sr, Ba, Pb), 20,45,46 which can affect the radiative transitions, the radiative decay time may have a distribution resulting in a multi-exponential decay. The long-lived component of the decay could correspond to Er³⁺ ions in a highly symmetric environment (cubic symmetry of the PbF₂ crystal structure), whereas the short-lived component corresponds to Er³⁺ ions in a less symmetric environment (corresponding to ion clusters). These two symmetries are distinguishable in luminescence decays due to the strong cross-relaxation of the 4S_{3/2} state. The strong cross-relaxation is expected for the cluster environment (with a shorter interionic distance), which strongly reduces the lifetime of the shortlived component. The two different environments are more difficult to detect for the ${}^4F_{9/2}$ and ${}^4I_{13/2}$ states because these states do not participate in cross-relaxation and the difference between the radiative lifetimes is hardly noticeable in experimental decays.

Analysis of the amplitude ratio (A_i) for the short-lived and long-lived components (Table S8, ESI†) for decays of ⁴S_{3/2} state allows us to understand which fraction of the Er3+ ions are distributed in the two crystalline environments. The crystals with the lowest doping concentration of Er1.5Yb1.5 and Er2Yb2 have comparable A_1 and A_2 values (amplitudes of the short-lived and long-lived components, respectively). In this case, the processing of the absorption spectra with the JO model probably gives an "average" value of the radiative lifetime, although the correctness of the application of the IO model for a material with two radiative lifetimes may be questionable. As the concentration of Yb3+ increases (Er2Yb3, Er2Yb5 and Er2Yb7.5 crystals), the number of Er3+ ions in the cluster fraction increases and becomes >95% for the Er2Yb5 crystal. Therefore, the Er2Yb5 crystal (with a dominant radiative lifetime) was chosen for further analysis of the correlations between IO calculations and experimental results.

Assuming that in the Er2Yb5 crystal (i) there is only one value of the radiative lifetime for each ${}^4S_{3/2}$, ${}^4F_{9/2}$ and ${}^4I_{13/2}$ state; (ii) there is a constant quenching rate for the ${}^4S_{3/2}$, ${}^4F_{9/2}$ and ⁴I_{13/2} states, where the quenching mechanism of the ⁴S_{3/2} state is cross-relaxation with the ground states (${}^{4}I_{15/2}$ or ${}^{2}F_{5/2}$); and (iii) the measurement artefact associated with the reabsorption of emitted photons is suppressed, the radiative lifetime, decay time, and quantum yield are bound by a simple equation:

$$\phi_{\rm DS} = \beta \frac{\tau}{\tau_{\rm rad}} \tag{2}$$

where β is the branching ratio, τ_{rad} is the radiative decay time calculated from the JO analysis and τ is the experimentally determined decay time.

Table 3 ϕ_{DS} (%) of some transitions in the PbF₂:Er³⁺,Yb³⁺ samples upon excitation of the ${}^{4}S_{3/2}$, ${}^{4}F_{9/2}$, $Er^{3+} \cdot {}^{4}I_{11/2}$ & $Yb^{3+} \cdot {}^{2}F_{7/2}$ and ${}^{4}I_{13/2}$ levels measured in an integrating sphere and corrected as described in Fig. S4 (ESI). Intensities of the 522 nm, 652 nm, 940 nm and 1495 nm lasers are 0.1 W cm^{-2} , 0.3 W cm^{-2} , 0.1 W cm^{-2} and 0.1 W cm^{-2} , respectively

Excitation	Emission	Er1.5Yb1.5	Er2Yb2	Er2Yb3	Er2Yb5	Er2Yb7.5
522 nm	${}^{4}S_{3/2} - {}^{4}I_{15/2}$	5.4	3.2	3.5	3.1	2.5
	$^{4}S_{3/2} - ^{4}I_{13/2}$	2.0	1.2	1.5	1.3	0.9
	${}^{4}\mathrm{F}_{9/2} - {}^{4}\mathrm{I}_{15/2}$	8.7	7.6	7.0	4.0	1.7
	$\{Er^{3+}:^{4}I_{11/2} \& Yb^{3+}:^{2}F_{7/2}\}$	46.7	51.9	57.0	48.3	42.0
652 nm	${}^{4}F_{9/2} - {}^{4}I_{15/2}$	22.0	23.5	28.2	24.7	23.4
	${}^{4}F_{9/2} - {}^{4}I_{15/2} $ { $Er^{3+} : {}^{4}I_{11/2} $ & Yb $^{3+} : {}^{2}F_{7/2}$ }	29.5	31.9	31.5	29.4	18.9
940 nm	${\rm Er^{3+}: ^4I_{11/2}\ \&\ Yb^{3+}: ^2F_{7/2}}$	37.3	60.6	69.4	52.9	43.2
	${}^{4}I_{13/2} - {}^{4}I_{15/2}$	3.0	4.4	4.5	2.7	3.0
1495 nm	$^4{\rm I}_{13/2} - ^4{\rm I}_{15/2}$	85.1	74.8	69.2	68.6	69.5

It is very likely that the conditions (i)-(iii) can be fulfilled for the ${}^4S_{3/2}$ - ${}^4I_{13/2}$ transition in the Er2Yb5 sample. Especially because this transition between two excited states is less affected by re-absorption. For example, Fig. S1c, and S3 (ESI†) indicate that there is a similar decay time for the ${}^4S_{3/2}$ $-{}^4I_{13/2}$ transition in the Er2Yb5 crystal and all powder mixtures prepared on the bases of this crystal. Taking into account the decay time (τ = 0.05 \pm 0.01 ms), the radiative lifetime ($\tau_{\rm rad}$ = 0.82 \pm 0.01 ms) and the branching ratio of β = 0.28 (Table S6, ESI†), eqn (2) allows to calculate the quantum yield of the ${}^4S_{3/2}$ $-{}^4I_{13/2}$ luminescence as $\phi_{\rm DS}$ = 1.4 \pm 0.3%, which agrees very well with the measured value of ϕ_{DS} = 1.3% (Table 3). When the same equation is applied to the ${}^4S_{3/2}$ - ${}^4I_{15/2}$ and ${}^4F_{9/2}$ - ${}^4I_{15/2}$ transitions, the calculation gives values of quantum yield of ϕ_{DS} = $3.3 \pm 0.07\%$ and ϕ_{DS} = 29.2 $\pm 4.7\%$ respectively. However, lower values of quantum yield of $\phi_{\rm DS}$ = 3.1% and $\phi_{\rm DS}$ = 24.7% (Table 3) have been measured experimentally using an integrating sphere and correction procedure in agreement to Wilson and Richards⁴⁷ (Fig. S4, ESI†). The $\phi_{
m DS}^*$ values before the correction as measured in an integrating sphere are given in Table S9 (ESI†). It is assumed that the difference between the quantum yields predicted (based on lifetime) and experimentally measured quantum yields - 3.3% vs. 3.1% (for the ${}^{4}\mathrm{S}_{3/2} - {}^{4}\mathrm{I}_{13/2}$ transition) and 29.2% vs. 24.7% (for the ${}^{4}\mathrm{F}_{9/2} - {}^{4}\mathrm{I}_{15/2}$ transition) - illustrates the realistic degree of agreement that can be expected between the JO calculations and the experimental result.

Given the results presented in Table 3, the probabilities of the transitions ${}^4S_{3/2} - {}^4F_{9/2}$ and $\{Er^{3+} : {}^4I_{11/2} \& Yb^{3+} : {}^2F_{7/2}\} - {}^4I_{13/2}$ can be also estimated from the values of ϕ_{DS} . Considering the model with three energy levels (0, 1 and 2) (Fig. S5, ESI†), the probability of transition (as the sum of radiative and non-radiative transitions) φ_{2-1} can be calculated using the quantum yields of the radiative transition (ϕ_{1-0}) at excitations (0-1) and (0-2):

$$\varphi_{2-1} = \frac{\phi_{1-0(0-2)}}{\phi_{1-0(0-1)}} \tag{3}$$

Table 4 Transition probabilities between certain Er³⁺ excited states in the PbF₂:Er³⁺,Yb³⁺ samples in the low excitation intensity range (0.1- $0.3~{\rm W}~{\rm cm}^{-2}$

φ_{2-1}	Er1.5Yb1.5	Er2Yb2	Er2Yb3	Er2Yb5	Er2Yb7.5
$^{4}S_{3/2}$ $^{-4}F_{9/2}$	0.40	0.32	0.25	0.14	0.07
$^{4}S_{3/2}$ $^{4}F_{9/2}$ $\{Er^{3+}: ^{4}I_{11/2} \& Yb^{3+}: ^{2}F_{7/2}\} - ^{4}I_{13/2}$	0.04	0.06	0.07	0.04	0.04

Since β for ${}^4S_{3/2} - {}^4F_{9/2}$ is very small – 3 \times 10⁻⁴, φ_{2-1} for the ${}^4S_{3/2}$ state represents the fraction of all excited ⁴S_{3/2} states that decay non-radiatively (via multi phonon relaxation) to the ⁴F_{9/2} state. In the case of $\{Er^{3+}: {}^{4}I_{11/2} \& Yb^{3+}: {}^{2}F_{7/2}\} - {}^{4}I_{13/2}$, β is unknown. Therefore, φ_{2-1} represents the fraction of all $\{Er^{3+} \cdot ^4I_{11/2} \& Yb^{3+} \cdot ^2F_{7/2}\}$ excited states that decay both radiatively and non-radiatively to the ⁴I_{13/2} state.

The data in Table 4 demonstrates that φ_{2-1} for the $\{Er^{3+}: {}^4I_{11/2}\}$ & Yb³⁺: ${}^{2}F_{7/2}$ \- ${}^{4}I_{13/2}$ transition is in the range of 0.04-0.07 for all Yb3+ concentrations and is slightly smaller than the probability for the ${}^{4}I_{11/2}$ radiative transition, since it has been shown that the branching ratio for the ${}^4I_{11/2} - {}^4I_{13/2}$ transition in Er³⁺ doped fluorides is in the range 0.11-0.15.33,48,49 In contrast. the φ_{2-1} value for the ${}^4S_{3/2} - {}^4F_{9/2}$ transition decreases with increasing Yb³⁺ concentration, indicating the predominance of cross-relaxation over non-radiative relaxation in crystals with high Yb3+ doping concentration.

Judd-Ofelt calculations for powder samples

JO calculations can help predicting parameters like radiative transition rates, branching ratios and even quantum efficiencies that can give an insight into the applicability of the materials. However, it is not always possible to obtain single crystals of the desired chemical composition for the IO analysis. In most cases, newly synthesized materials are obtained in a form of micro- or nanoparticles. For such samples, it is not easy to obtain the absorption cross-section for the JO method as it first requires determination of the absorption coefficient that in turn can be defined if the light propagation path is known. Instead, powder samples are usually treated using excitation⁵⁰ and diffuse reflection⁵¹⁻⁵³ spectra. We assumed that the accuracy of IO calculations for a powder sample can be evaluated if the result of JO calculations for the equivalent crystal is already known. To test this approach a part of the Er2Yb5 crystal was ground into microparticles, followed by measurements of excitation and diffuse reflectance spectra.

In the case of Er3+ ions, all methods of JO analysis of powder samples use the luminescence decay time of the ${}^4I_{13/2}$ $-{}^4I_{15/2}$ transition to calibrate the JO parameters Ω_t . It is assumed that the luminescence decay time of the ${}^4I_{13/2} - {}^4I_{15/2}$ transition is equal to the radiative lifetime and that the $\phi_{\rm DS}$ of the $^4{
m I}_{13/2}$ -⁴I_{15/2} transition is equal to 100% upon the excitation of the ⁴I_{13/2} state. However, this assumption does not take into account the various quenching processes that can take place in the non-ideal sample. In order to quantify this effect, the $\phi_{\rm DS}$ of the ${}^4I_{13/2}$ $-{}^4I_{15/2}$ transition was determined using 1495 nm excitation, giving a value of 68.8%. Furthermore, the results of

the previous section clearly show that the decay times obtained for the crystal and for the powder with the same chemical composition differ significantly due to reabsorption effect.⁵⁴ The decay time of the ${}^4I_{13/2}$ - ${}^4I_{15/2}$ transition in the Er2Yb5 crystal is 8.8 ms whereas the same transition in the powder has a decay time of 7.4 ms (5.4 ms for the diluted powder (Fig. 2(f))). It can be also noted that the experimentally measured lifetime in the crystal exceeds the radiative lifetime obtained from the IO analysis, which is 8.4 ms.

Using eqn (1) (with $\beta = 1$) it is possible to determine experimentally that the radiative lifetime of the ${}^4I_{13/2} - {}^4I_{15/2}$ transitions as 7.9 ms (given ϕ_{DS} = 68.6% and τ = 5.4 ms), which is in the good agreement with the value of 8.4 ms obtained from the JO calculations for the crystal. The results lead to a rather curious observation: quenching decreases the luminescence decay time, whereas reabsorption increases it. Thus, the experimental decay time for the powder (7.4 ms) is only coincidently close to the radiation lifetime predicted by IO theory (8.4 ms) for the single crystal. For the sake of simplicity, the value of 8.4 ms (calculated using JO theory for the crystal) was taken as the radiative lifetime in the further calculations for the powder sample.

With the radiative lifetime of the ${}^4I_{13/2} - {}^4I_{15/2}$ transition is defined (8.4 ms), it is now possible to perform the IO calculations on powder samples. First, the Method A described in the paper⁵⁰ was tested. It uses the excitation spectrum recorder while monitoring the emission of the ${}^4S_{3/2}$ – ${}^4I_{15/2}$ transition. The spectrum obtained is given in Fig. 4(a). Using the transitions marked with arrows, the JO parameters Ω_t were calculated in arbitrary units and then recalculated using the radiative lifetime (8.4 ms) of the ${}^{4}I_{13/2}$ - ${}^{4}I_{15/2}$ transition established above. These parameters were then used to estimate the transition probabilities and radiative lifetimes of other transitions. The algorithm of this method is illustrated in Fig. S6a (ESI†).

Secondly, the Method B described in the paper⁵¹ was evaluated. This approach uses the diffuse reflectance spectrum of the powder sample. The spectrum obtained is presented in Fig. 4(b). The band located around 800 nm was excluded from the calculation due to its extremely low signal to noise ratio. The band with a maximum at 980 nm was also not included in the calculations because the observed absorption band is an overlap of the ${}^4I_{11/2} - {}^4I_{15/2}$ transition of Er^{3+} ions and the ${}^{2}F_{7/2}$ $-{}^{2}F_{5/2}$ transition of Yb³⁺ ions. To convert from arbitrary units of the diffuse reflectance spectrum to cm² of the absorption cross-section, the experimentally determined oscillator strength of the 4I15/2-4I13/2 transition is calibrated to the radiative lifetime of the ${}^4I_{13/2}$ – ${}^4I_{15/2}$ transition. The treated spectrum is then used to calculate the JO parameters Ω_t . The algorithm of this method is illustrated in Fig. S6b (ESI†).

The final approach that was tested was Method C described in ref. 52,53. Unlike the previous case, here the absorption in arbitrary optical density units is used to calculate the relative intensity parameters. The actual JO parameters Ω_t are calculated afterwards using the radiative lifetime of the ${}^4I_{13/2} - {}^4I_{15/2}$ transition. In this case, a diffuse reflectance spectrum was used in combination with Kubelka-Munk theory to perform the

PCCP Paper

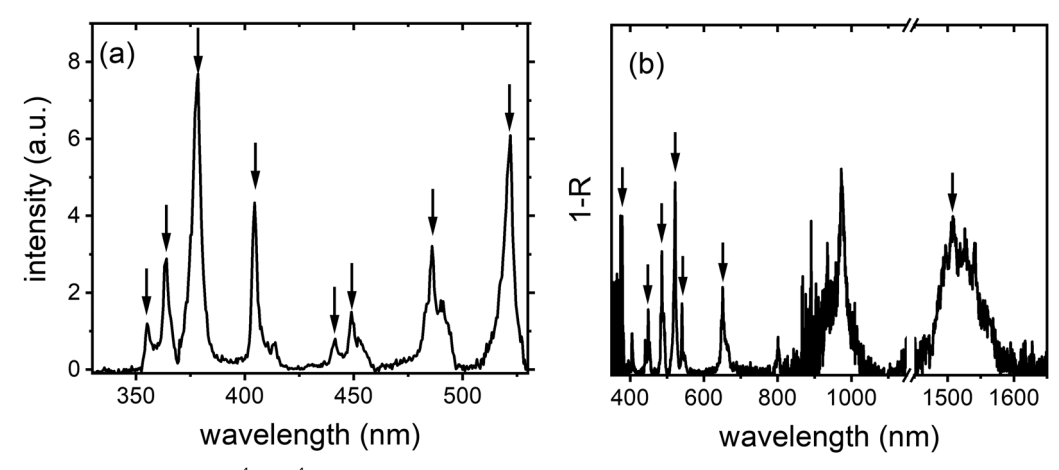


Fig. 4 (a) The excitation spectrum of the ${}^4S_{3/2} - {}^4I_{15/2}$ transition (detection at 540 nm); (b) the reflectance (R) spectrum of the Er2Yb5 powder sample. The arrows indicate the bands used to calculate the Judd-Ofelt parameters

calculations in arbitrary units. The algorithm of this method is illustrated in Fig. S6c (ESI†).

In order to compare the results obtained using these three different methods the RMS values of the radiative lifetimes and Ω_t values obtained for the crystalline and powder samples were calculated (Table 5). The results of lifetimes in Table 5 and the comparison branching ratios in Table S10 (ESI†) clearly show the difference between the three methods. Although none of these approaches provide a 100% consistency between transition probabilities, the Method A⁵⁰ as well as Method C^{52,53} show adequate agreement between values calculated on a single crystal sample and results obtained on powder. If the difference in Ω_t values and branching ratios is also taken into account, then the Method C52,53 is preferred. It should also be noted that the radiative lifetimes of the weak ${}^4I_{9/2} - {}^4I_{15/2}$ transition show the greatest difference between the methods. This state has a lower absorption and emission intensity as well as a worse agreement between experimental and calculated transition probabilities compared to other emissive excited

Table 5 Comparison of the radiative lifetime of Er2Yb5 powder obtained with different approaches based on the JO theory

	Lifetime, ms					
Emission band	Crystal Method A ⁵⁰		Method B ⁵¹	Method C ^{52,53}		
$^{4}G_{9/2}$ $^{4}I_{15/2}$	0.56	0.40	0.58	0.50		
$^{2}H_{11/2} - ^{4}I_{15/2}$	0.62	0.35	0.89	0.77		
$^{4}S_{3/2} - ^{4}I_{15/2}$	0.82	0.73	0.71	0.61		
$^{4}F_{9/2} - ^{4}I_{15/2}$	1.03	0.51	1.66	1.43		
$^{4}I_{9/2} - ^{4}I_{15/2}$	8.42	3.81	17.56	14.69		
$^{4}I_{11/2}$ $-^{4}I_{15/2}$	9.02	8.44	9.01	7.26		
${}^{4}I_{13/2} - {}^{4}I_{15/2}$	8.17	8.19	12.71	8.09		
Relative RMS		0.91	1.44	0.94		
(with ⁴ I _{9/2})						
Relative RMS		0.73	0.95	0.57		
$(w/o^{-4}I_{9/2})$						
Judd-Ofelt paran	neters, ×	10^{-20} cm^2				
Ω_2	0.95	1.08	0.68	0.73		
Ω_4	0.12	1.79	0.31	0.34		
Ω_6	1.14	0.95	1.00	1.08		
Relative RMS		2.86	0.74	0.67		

states of the Er³⁺.⁴⁹ However, excluding this transition from the calculation of RMS (Table 5) did not change the conclusion that the method described in Method C52,53 better fits the parameters calculated for the single crystal.

As an additional proof, the same procedure was carried out with the Er2Yb2 crystal. Similarly, to the Er2Yb5 the JO calculations are first performed with the material in the form of a crystal, which was then ground to powder and the same three methods are tested. The results obtained are presented in Fig. S7 (ESI†), as well as Tables S11 and S12 (ESI†). The data allow the same conclusions to be drawn: Method C52,53 gave better agreement between the values obtained on a crystal sample and on a powder sample.

Up-conversion luminescence in PbF₂:Er³⁺,Yb³⁺ crystals

Knowing the $\phi_{
m DS}$ of the $^4{
m S}_{3/2}$ and $^4{
m F}_{9/2}$ emitting states and the decay times of the ${}^{4}I_{11/2}$ & $Yb^{3+}:{}^{2}F_{7/2}$ and ${}^{4}I_{13/2}$ intermediate states, one can estimate the efficiency of the UC process based on excited state energy transfer. In general, $\phi_{\rm UC}$ should be less than or equal to $0.5\phi_{\rm DS}$ as UC is a two- or three-photon process. In addition, the longer decay time of $\{^4I_{11/2} \& Yb^{3+}: ^2F_{7/2}\}$ and ⁴I_{13/2} states provides a greater probability of UC at lower excitation intensities, which is important for many applications.

Fig. 5(a) demonstrates the upconversion emission spectra under 976 nm excitation with an intensity of 350 W cm⁻², where all spectra are normalised to the maximum intensity of the ${}^4F_{9/2}$ – ${}^4I_{15/2}$ transition. First, the UC properties of the crystals were investigated experimentally using a direct approach: $\phi_{\rm UC}$ was measured in the integrating sphere at different excitation intensities of the 976 nm laser. It is important to note that the results of measurements of $\phi_{\rm UC}$ can be biased in a number of ways.⁵⁵ First, at high intensities the samples can heat up, reducing the emission intensity. Second, the emission can be reabsorbed by the sample as it propagates trough the integrating sphere, reducing the luminescence. The last major source of the error in the estimation of the $\phi_{\rm UC}$ is related to the geometry of the sample. During propagation through the sample, the excitation intensity is being absorbed. This leads to a decrease in the incident intensity inside the sample, and

PCCP Paper

due to the non-linear nature of the up-conversion process, a decrease in observed $\phi_{\rm UC}$.

The first problem can be solved by estimating the temperature of the sample from the ratio of the 2H11/2-4I15/2 and ${}^4\mathrm{S}_{3/2} - {}^4\mathrm{I}_{15/2}$ emission bands, which are thermally coupled. The temperature can be calculated as

$$\frac{1}{T} = \frac{1}{T_0} - \frac{k_B}{\Delta E} \cdot \ln \left(\frac{I_{520} I_{550}^0}{I_{550} I_{520}^0} \right) \tag{4}$$

where $k_{\rm B}$ is the Boltzmann constant, ΔE is the energy difference between the ${}^{2}H_{11/2}$ and ${}^{4}S_{3/2}$ levels, I_{520} and I_{550} is the emission intensities of the ${}^{2}H_{11/2}$ and ${}^{4}S_{3/2}$ levels respectively, T_{0} is the initial temperature in the absence of excitation and I_{550}^0 and I_{550}^0 are the emission intensities at the initial temperature.

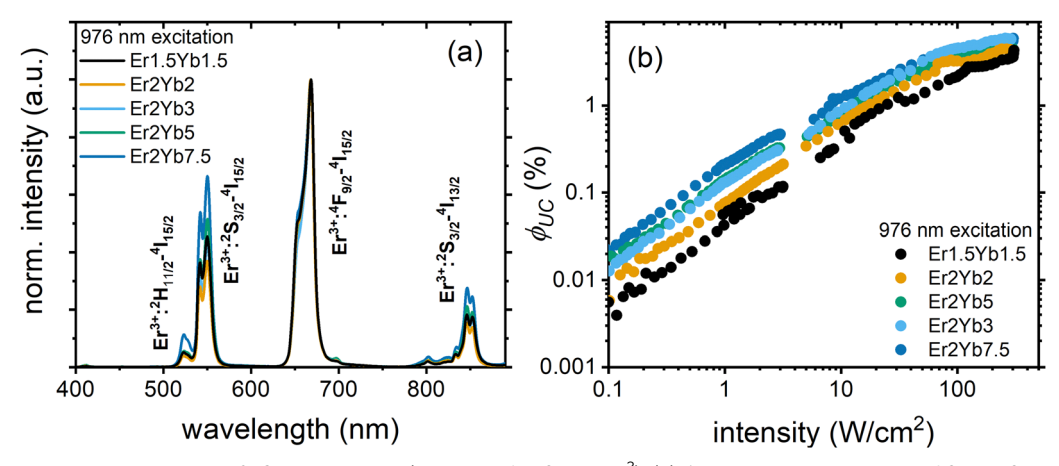
The procedure was described in detail in the literature⁵⁶ and the results of the calculation with eqn (4) are displayed in Fig. S8 (ESI†). It can be seen that only in the sample with the highest concentration of Yb3+ (Er2Yb7.5) there is noticeable change in the temperature of the sample.

The problem of re-absorption within the integrating sphere can be solved as described previously for ϕ_{DS} in Table 3 and Fig. S4 (ESI†). Finally, in order to account for the effect of sample size on the calculated $\phi_{\rm UC}$ values, several assumptions should be made. A crystalline sample of a given thickness is considered to be a seamless stack of 100 layers. The ϕ_{UC} of each layer was assumed to be $\phi_{\rm UC} \propto I^n$ where I is the incident intensity and n is varied from 0 to 1 in 0.1 steps to illustrate different power dependencies of $\phi_{\rm UC}$. It is then possible to calculate the number of incident and absorbed photons for each layer as well as the $\phi_{\rm UC}$ of the layer. Combination of these two values (ϕ_{UC} and n) gives the number of photons emitted by each layer. By summing the emitted and absorbed photons in each layer, the $\phi_{\rm UC}$ of the sample can be calculated based on measured $\phi_{\rm UC}$ (Fig. S9, ESI†).

The ϕ_{UC} values after the above-mentioned corrections (similar to the detailed explanation given by Madirov et al. 55) are presented in the Fig. 5(b). The data in Fig. 5(b) indicate that $\phi_{\rm UC}$ increases as the incident intensity increases, reaching its maximum value of 5.9% observed at 350 W cm⁻² for the Er2Yb3 crystal. It is known that the synthesis of PbF2 single crystals by the Bridgman method can lead to a certain amount of defects in the crystal lattice,⁵⁷ which could quench the emission. As a result, it might lead to slightly lower observed ϕ_{UC} values compared to SrF₂:Er³⁺,Yb³⁺ (6.5%)¹⁶ and BaF₂:Er³⁺,Yb³⁺ $(9.9\%)^{19}$ crystals. As in BaF₂:Er³⁺,Yb³⁺ and SrF₂:Er³⁺,Yb³⁺, at low intensities (<10 W cm⁻²) the highest $\phi_{\rm UC}$ is observed in the samples with the maximum amount of the Yb^{3+} ions (7.5%), whereas at higher intensities (>10 W cm⁻²) samples with a lower concentration (3%) of Yb³⁺ demonstrate the highest ϕ_{UC} .

The experimental dependence of $\phi_{\rm UC}$ on excitation intensity can be examined using the approach proposed by Joseph et al. in order to estimate a single figure of merit parameter of the UC process - critical power density (CPD).³² Based on the CPD value, other important parameters of the UC process - the maximum value of the quantum yield $(\phi_{ ext{UCsat}})$ and the energy transfer rate between donor and acceptor ions (k_{12}) can be derived.32 It should be noted that the CPD concept was derived for a two-photon UC process (such as population and emission from the ⁴S_{3/2} state) and not for a three-photon process (which sometimes refers to emission from the ⁴F_{9/2} state). Table 6 displays experimental values of the UC quantum yield at a maximum intensity of 350 W cm⁻² (Max ϕ_{UC}), the values of the CPD, the values of $\phi_{\text{UC CPD}}$ (UC quantum yield at an intensity corresponding to the CPD), as well as ϕ_{UCsat} , and k_{12} derived from the CPD.

The following conclusions can be drawn from the data in Table 6. The CPD value decreases as the concentration of the Yb³⁺ ions increases and reaches 9.2 W cm⁻² for the Er2Yb7.5 sample. Slightly lower CPD values ($\sim 1 \text{ W cm}^{-2}$) have previously been reported for the most efficient hosts (NaYF4, YF3, YCl3, and La2O3) 32. However, these lower values were observed at a much higher concentration of Yb3+ (18%). Thus, a high concentration of Yb³⁺ is preferred to obtain a high quantum yield at a lower excitation intensity. In contrast, the highest value of ϕ_{UCsat} is expected for the sample with the lowest doping concentration (Er1.5Yb1.5), the sample with the lowest probability of the cross-relaxation. It is interesting to note that



(a) UC emission spectra under the 976 nm excitation (intensity of 350 W cm⁻²); (b) $\phi_{\rm UC}$ in the intensity range of 0.1–350 W cm⁻².

Paper

Table 6 Maximum (at 350 W cm $^{-2}$) $\phi_{\rm UC}$ values for UC emission in the 400–900 nm range (Max $\phi_{\rm UC}$ total) and for the ${}^4{\rm S}_{3/2} - {}^4{\rm I}_{15/2}$ emission (Max ϕ_{UC} $^4S_{3/2}$ $^{-4}I_{15/2}$); CPD; ϕ_{UC} at CPD (ϕ_{UC} CPD); and saturation ϕ_{UC} (ϕ_{UCsat}) as well as energy transfer rate (k_{12}) of the ${}^{4}\text{S}_{3/2} - {}^{4}\text{I}_{15/2}$ transition

	Er1.5Yb1.5	Er2Yb2	Er2Yb3	Er2Yb5	Er2Yb7.5
	4.3	4.4	5.9	4.7	5.8
Max $\phi_{\rm UC}$ $^4S_{3/2}$ $^{-4}I_{15/2}$, %	1.0	0.9	1.2	1.1	1.3
CPD ${}^{4}S_{3/2} - {}^{4}I_{15/2}$, W cm ⁻²	48.4	37.9	17.8	16.0	9.2
$\phi_{\text{UC CPD}}$, %	0.4	0.3	0.4	0.2	0.2
	2.7	1.3	2.6	1.2	1.3
k_{12} , $\times 10^{-17}$ cm ³ s ⁻¹	0.6	1.5	2.1	1.9	5.4

 ϕ_{UCsat} (Table 6) is 0.5 ϕ_{DS} (Table 3) for most samples, with a slightly larger deviation for Er2Yb7.5. Furthermore, it could be assumed that in the case of the ${}^4S_{3/2}$ state, the relatively low ϕ_{DS} is a limiting factor for achieving high ϕ_{UC} .

While it is well known that the green UC emission from the ⁴S_{3/2} state is a two-photon process, the red UC emission from the ⁴F_{9/2} state may have a more complex origin. It is hypothe sized that if the ${}^{4}F_{9/2}$ state is populated *via* relaxation of the ⁴S_{3/2} state (and also a two-photon process), the red-to-green (R/G) ratio in the UC spectra should be similar to the R/G ratio observed for the direct excitation of the ⁴S_{3/2} state. In the latter case, the R/G ratio can be estimated from the values of ϕ_{DS} given in Table 3. Therefore, a comparison of the R/G ratios for the UC and DS processes should shed light on the mechanism of the ⁴F_{9/2} state population. Fig. 6(a) demonstrates how the R/G ratio changes as a function of excitation intensity in the UC process for the Er2Yb5 sample. At low excitation intensities $(<1 \text{ W cm}^{-2})$, the R/G ratio in the UC spectra corresponds well to the R/G value obtained by direct excitation of the ⁴S_{3/2} state (R/G = 1.5). It is therefore likely that the ${}^4F_{9/2}$ state originates from the ⁴S_{3/2} state via non-radiative relaxation. However, increasing the excitation intensity (>1 W cm⁻²) clearly leads to an increase in the R/G ratio. This rise in red emission can be explained either by the model proposed by Berry and May,⁵⁸ where the ⁴F_{9/2} state results from the three-photon process of

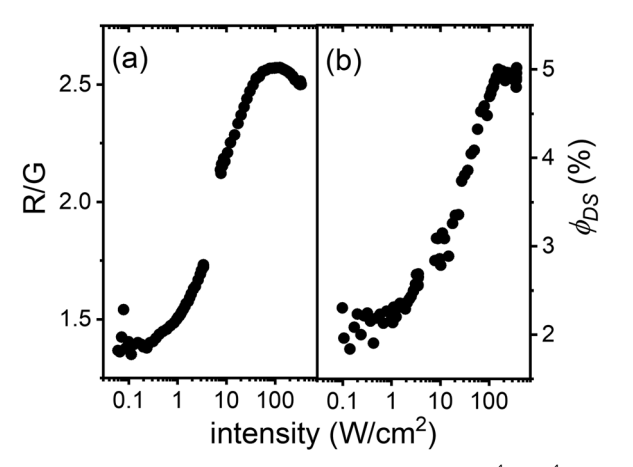


Fig. 6 Er2Yb5 sample: (a) ratio of the intensities of the ${}^4F_{9/2} - {}^4I_{15/2}$ (red) transition and the ${}^4S_{3/2} - {}^4I_{15/2}$ (green) transition as a function of 976 nm excitation intensity in the 0.1–350 W cm $^{-2}$; (b) $\phi_{\rm DS}$ of the Er $^{3+}$: 4 I $_{13/2}$ - 4 I $_{15/2}$ transition as a function of intensity at 940 nm excitation.

populating the ²H_{9/2} state and the subsequent back energy transfer to Yb³⁺, or by the ETU process involving ⁴I_{13/2} state.

In turn, the 4I13/2 state can stem either by radiative transition from the ${}^4I_{11/2}$ or ${}^2S_{3/2}$ states, or by cross-relaxation of the ${}^4S_{3/2}$ state. The probability of the ${}^4I_{11/2}$ - ${}^4I_{13/2}$ transition (0.04) was calculated earlier in Table 4 as the contribution of both radiative and phonon-assisted relaxation processes. This probability does not depend on the excitation intensity and, thus $\phi_{\rm DS}$ of the ${}^4{\rm I}_{11/2} - {}^4{\rm I}_{15/2}$ radiative process should also remain constant. However, an interesting observation can be found in Fig. 6(b). The quantum yield of the ${}^{4}I_{11/2}-{}^{4}I_{15/2}$ luminescence increases with increasing laser intensity, suggesting that the $^{4}I_{13/2}$ state is populated *via* a new pathway at high excitation intensity - mainly via cross-relaxation of the 2S1/2 state and minimally via the ${}^{2}S_{3/2}$ $-{}^{4}I_{13/2}$ radiative transition. Although it is rather difficult to decide how the 4F9/2 state is populated either via the Berry and May model or via the ${}^4I_{13/2}$ state – it can be assumed that the sublinear increase in the number of ⁴I_{13/2} states with excitation intensity leads to an increase in the number of ${}^4F_{9/2}$ states (by the ETU process: ${}^4I_{13/2}$ + ${}^2F_{5/2}$ \rightarrow ${}^4F_{9/2}$ + ${}^2F_{7/2}$) and thus to an increase in the R/G ratio. Fig. S11 (ESI†) also demonstrates the similar trends in the R/G ratio and $\phi_{\rm DS}$ for other investigated samples. Thus, the assumption made about additional population of the ⁴F_{9/2} state via ⁴I_{13/2} state can be valid for a wide range of Yb³⁺ concentrations (1.5-7.5%).

Conclusions

The optical properties of a series of crystalline PbF₂:Er³⁺,Yb³⁺ samples (with fixed Er³⁺ concentration of 2 mol% and variable Yb³⁺) concentration of (2–7.5 mol%) were investigated. Since the luminescence properties of the ${}^4S_{3/2}$ and ${}^4F_{9/2}$ states of Er $^{3+}$ are important for understanding of the UC in PbF₂:Er³⁺,Yb³⁺ crystals, they were investigated by applying JO analysis, luminescence decay measurements and determination of the absolute luminescence quantum yield at the direct excitation of the corresponding states. It was shown that the quantum yield of the ${}^4S_{3/2}$ and ${}^4F_{9/2}$ states can be predicted using the JO model and luminescence decays, and that these values are in good conformity with experimental values of quantum yield measured by an integrating sphere. In the case study for the Er2Yb5 crystal, ϕ_{DS} values of 3.3% (${}^4S_{3/2}$ – ${}^4I_{15/2}$ transition) and 29.2% $({}^{4}F_{9/2} - {}^{4}I_{15/2}$ transition) were obtained from the JO model, while 3.1% and 24.7%, respectively, were measured using an integrating sphere. The proposed method can also be applied to other upconversion materials doped with rare earth ions (Tm3+ and Ho³⁺), as long as it is possible to perform Judd-Ofelt analysis for the emitting ions and obtain luminescence decay times. Upon excitation with a 976 nm laser, all PbF₂:Er³⁺,Yb³⁺ crystals exhibit bright UC emission. In the case study for the Er2Yb5 crystal, the value of ϕ_{UCsat} for the ${}^{4}\text{S}_{3/2}$ - ${}^{4}\text{I}_{15/2}$ transition was estimated to be 1.2%. This value follows an empirical rule $\phi_{\rm UCsat} \approx 0.5\phi_{\rm DS}$, leading to the conclusion that the pure emission property of the 4S3/2 state is the limiting factor for a UC quantum yield. Overall, $\phi_{\rm UC}$ can be as high as 4.4% for the

Er2Yb5 crystal (at intensity of 350 W cm⁻²) because it also includes the ${}^4F_{9/2}$ - ${}^4I_{15/2}$ transition with much higher ϕ_{DS} . The ⁴F_{9/2} state originates from the ⁴S_{3/2} via multi phonon relaxation (with probability of 0.136 for the Er2Yb5 sample) or via the ETU from the ⁴I_{13/2} state or *via* the ²H_{9/2} state. This complex path reduces the ϕ_{UC} for the ${}^4\mathrm{F}_{9/2}{}^{-4}\mathrm{I}_{15/2}$ transition, although the emission property of the ${}^4F_{9/2}$ state is good. The highest value of $\phi_{\rm UC}$ 5.9% was measured for the Er2Yb3 crystal in the sample series.

UC materials are often not available in the form of transparent crystals, but are synthesized as microcrystalline or nanocrystalline powders. Several methods of JO parameters calculation for powder samples are available in the literature. In the present work, comparison of three methods (for powder samples) with results obtained for a single crystal of identical material was done. The RMS analysis reveals that method, ^{52,53} utilizing the reflection spectrum and giving Ω_t parameters measured in arbitrary units, gives better agreement between the results obtained for the crystal and the powder. The true values of Ω_t (in cm²) were then recovered by the known value of radiative lifetime for the ${}^4I_{13/2}$ – ${}^4I_{15/2}$ transition. However, it has been demonstrated that the radiative lifetime of the ${}^4I_{13/2}$ – ${}^4I_{15/2}$ transition cannot simply be considered equal to the measured decay time of the 4I13/2-4I15/2 transition, as very often due to the non-perfect crystalline materials and the presence of additional quenching channels $\phi_{\rm DS} < 100\%$. More careful data evaluation of radiative rate for the ${}^4I_{13/2}-{}^4I_{15/2}$ transition is therefore required before applying decay time of the ${}^4I_{13/2}$ – ${}^4I_{15/2}$ transition in the IO analysis.

Although $\phi_{\rm UC}$ of PbF₂:Er³⁺,Yb³⁺ crystals does not outperform $SrF_2:Er^{3+},Yb^{3+}$ ($\phi_{UC} = 6.5\%$) and $BaF_2:Er^{3+},Yb^{3+}$ ($\phi_{UC} = 10.0\%$) crystal series, the comprehensive data set presented in our work for PbF2:Er3+,Yb3+ crystals can contribute to a better understanding of UC phenomena and provide a reference data set for the use of UC materials in practical applications.

Conflicts of interest

There are no conflicts to declare.

Acknowledgements

The reported study was funded DFG (project no. TU 487/8-1 for A. T. and B. S. R.). The financial support provided by the Helmholtz Association is gratefully acknowledged: (1) a Recruitment Initiative Fellowship for B. S. R.; (2) the funding of chemical synthesis equipment from the Helmholtz Materials Energy Foundry (HEMF); and (3) Research Field Energy— Program Materials and Technologies for the Energy Transition-Topic 1 Photovoltaics. The authors acknowledge T. Bergfeldt (IAM, KIT) for conducting WDXRF analysis.

References

1 R. Singh, E. Madirov, D. Busko, I. M. Hossain, V. A. Konyushkin, A. N. Nakladov, S. V. Kuznetsov, A. Farooq,

- S. Gharibzadeh, U. W. Paetzold, B. S. Richards and A. Turshatov, ACS Appl. Mater. Interfaces, 2021, 13, 54874-54883.
- 2 Q. Li, J. Lin, J. Wu, Z. Lan, Y. Wang, F. Peng and M. Huang, Electrochim. Acta, 2011, 56, 4980-4984.
- 3 B. S. Richards, D. Hudry, D. Busko, A. Turshatov and I. A. Howard, Chem. Rev., 2021, 121, 9165-9195.
- 4 N. Katumo, K. Li, B. S. Richards and I. A. Howard, Sci. Rep., 2022, 12, 2100.
- 5 A. Baride, J. M. Meruga, C. Douma, D. Langerman, G. Crawford, J. J. Kellar, W. M. Cross and P. S. May, RSC Adv., 2015, 5, 101338.
- 6 J. Zhu, S. Wang, Z. Yang, S. Liao, J. Lin, H. Yao, F. Huang, Y. Zheng and D. Chen, Nanoscale, 2022, 14, 3407-3415.
- 7 S. Wang, J. Lin, Y. He, J. Chen, C. Yang, F. Huang and D. Chen, Chem. Eng. J., 2020, 394, 124889.
- 8 M. S. Pudovkin, S. L. Korableva, D. A. Koryakovtseva, E. V. Lukinova, A. V. Lovchev, O. A. Morozov and V. V. Semashko, J. Nanopart. Res., 2019, 21, 266.
- 9 C. D. S. Brites, S. Balabhadra and L. D. Carlos, Adv. Opt. Mater., 2019, 7, 1801239.
- 10 J. Woidasky, I. Sander, A. Schau, J. Moesslein, P. Wendler, D. Wacker, G. Gao, D. Kirchenbauer, V. Kumar, D. Busko, I. A. Howard, B. S. Richards, A. Turshatov, S. Wiethoff and C. Lang-Koetz, Resour., Conserv. Recycl., 2020, 161, 104976.
- 11 F. Auzel, Chem. Rev., 2004, 104, 139-174.
- 12 I. Etchart, A. Huignard, M. Bérard, M. N. Nordin, I. Hernández, R. J. Curry, W. P. Gillin and A. K. Cheetham, J. Mater. Chem., 2010, 20, 3989-3994.
- 13 M. Kaiser, C. Würth, M. Kraft, I. Hyppänen, T. Soukka and U. Resch-Genger, Nanoscale, 2017, 9, 10051-10058.
- 14 M. Pokhrel, G. A. Kumar and D. K. Sardar, J. Mater. Chem. A, 2013, 1, 11595-11606.
- 15 G. Wang, Q. Peng and Y. Li, J. Am. Chem. Soc., 2009, 131, 14200-14201.
- 16 D. Saleta Reig, B. Grauel, V. A. Konyushkin, A. N. Nakladov, P. P. Fedorov, D. Busko, I. A. Howard, B. S. Richards, U. Resch-Genger, S. V. Kuznetsov, A. Turshatov and C. Würth, J. Mater. Chem. C, 2020, 8, 4093-4101.
- 17 S. Kuznetsov, Y. Ermakova, V. Voronov, P. Fedorov, D. Busko, I. A. Howard, B. S. Richards and A. Turshatov, J. Mater. Chem. C, 2018, 6, 598-604.
- 18 S. Balabhadra, M. F. Reid, V. Golovko and J.-P. R. Wells, J. Alloys Compd., 2020, 834, 155165.
- 19 E. I. Madirov, V. A. Konyushkin, A. N. Nakladov, P. P. Fedorov, T. Bergfeldt, D. Busko, I. A. Howard, B. S. Richards, S. V. Kuznetsov and A. Turshatov, J. Mater. Chem. C, 2021, 9, 3493-3503.
- 20 S. V. Chernov, W. Gunßer and I. V. Murin, Solid State Ionics, 1991, 47, 67-70.
- 21 R. Reisfeld and C. K. Jørgensen, Lasers and Excited States of Rare Earths, Springer Berlin Heidelberg, Berlin, Heidelberg, 1977, pp. 1-63, DOI: 10.1007/978-3-642-66696-4_1.
- 22 J. M. O'Hare, J. Chem. Phys., 1972, 57, 3838-3843.
- 23 S. I. Mho and J. C. Wright, J. Chem. Phys., 1983, 79, 3962-3975.

- 24 D. G. Mead and G. R. Wilkinson, J. Phys. C-Solid State Phys., 1977, 10, 1063-1072.
- 25 H. Wu, Z. Hao, L. Zhang, X. Zhang, Y. Xiao, G.-H. Pan, H. Wu, Y. Luo, H. Zhao and J. Zhang, J. Phys. Chem. C, 2018, 122, 9611-9618.
- 26 M. J. Weber, Phys. Rev., 1967, 157, 262-272.
- 27 S. A. Miller, H. E. Rast and H. H. Caspers, J. Chem. Phys., 1970, 52, 4172-4175.
- 28 R. Moncorge, Ann. Chimie Sci. Materiaux, 2003, 28, 5-20.
- 29 P. Zhang, J. Yin, B. Zhang, L. Zhang, J. Hong, J. He and Y. Hang, Opt. Lett., 2014, 39, 3942-3945.
- 30 S. V. Kuznetsov and P. P. Fedorov, Inorg. Mater., 2008, 44, 1434-1458.
- 31 I. I. Buchinskaya and P. P. Fedorov, Russ. Chem. Rev., 2004, 73, 371-400.
- 32 R. E. Joseph, C. Jiménez, D. Hudry, G. Gao, D. Busko, D. Biner, A. Turshatov, K. Krämer, B. S. Richards and I. A. Howard, J. Phys. Chem. A, 2019, 123, 6799-6811.
- 33 D. K. Sardar, W. M. Bradley, J. J. Perez, J. B. Gruber, B. Zandi, J. A. Hutchinson, C. W. Trussell and M. R. Kokta, J. Appl. Phys., 2003, 93, 2602-2607.
- 34 J. Bergstrand, Q. Liu, B. Huang, X. Peng, C. Würth, U. Resch-Genger, Q. Zhan, J. Widengren, H. Ågren and H. Liu, Nanoscale, 2019, 11, 4959-4969.
- 35 M. P. Hehlen, M. G. Brik and K. W. Krämer, J. Lumin., 2013, 136, 221-239.
- 36 I. Camarillo, E. Camarillo, F. Ramos, M. Flores and U. Caldiño, J. Phys.: Condens. Matter, 2004, 16, 5925.
- 37 W. T. Carnall, H. Crosswhite and H. M. Crosswhite, Energy level structure and transition probabilities in the spectra of the trivalent lanthanides in LaF3, United States, 1978.
- 38 I. H. Malitson and M. J. Dodge, J. Opt. Soc. Am., 1969, 59, 500A.
- 39 Y. Zhang, J.-M. Liu, M.-H. Liu, Z.-B. Zhang, W.-H. Wong and D.-L. Zhang, Spectrochim. Acta, Part A, 2020, 239, 118536.
- 40 C. Görller-Walrand and K. Binnemans, HPCRE, Elsevier, 1998, vol. 25, pp. 101-264.
- 41 E. Fišerová and M. Kubala, J. Lumin., 2012, 132, 2059-2064.
- 42 C. de Mello Donegá, A. Meijerink and G. Blasse, J. Lumin., 1994, 62, 189-201.

- 43 F. T. Rabouw, P. T. Prins, P. Villanueva-Delgado, M. Castelijns, R. G. Geitenbeek and A. Meijerink, ACS Nano, 2018, 12, 4812-4823.
- 44 A. Baride, P. S. May, Jr. and M. T. Berry, J. Phys. Chem. C, 2020, 124, 2193-2201.
- 45 F. Ma, F. Su, R. Zhou, Y. Ou, L. Xie, C. Liu, D. Jiang, Z. Zhang, Q. Wu and L. Su, Mater. Res. Bull., 2020, 125, 110788.
- 46 A. Gektin, N. Shiran, V. Nesterkina, Y. Boyarintseva, V. Baumer, G. Stryganyuk, K. Shimamura and E. Villora, J. Lumin., 2009, 129, 1538-1541.
- 47 L. R. Wilson and B. S. Richards, Appl. Opt., 2009, 48, 212-220.
- 48 H. Ebendorff-Heidepriem, D. Ehrt, M. Bettinelli and A. Speghini, J. Non-Cryst. Solids, 1998, 240, 66-78.
- 49 G. Yao, C. Lin, Q. Meng, P. Stanley May and M. T. Berry, J. Lumin., 2015, 160, 276-281.
- 50 W. Luo, J. Liao, R. Li and X. Chen, Phys. Chem. Chem. Phys., 2010, 12, 3276-3282.
- 51 Y. Zhang, B. Chen, S. Xu, X. Li, J. Zhang, J. Sun, X. Zhang, H. Xia and R. Hua, Phys. Chem. Chem. Phys., 2018, 20, 15876-15883.
- 52 E. Cantelar, M. Marin-Dobrincic, T. Jardiel, A. C. Caballero and F. Cussó, Opt. Mater., 2015, 41, 122-125.
- 53 A. Egaña, M. Tardío, C. de la Torre-Gamarra, A. Várez, E. Cantelar and J. E. Muñoz Santiuste, J. Lumin., 2018, 202, 232-238.
- 54 J.-F. Cormier, M. Fortin, J. Frechette, I. Noiseux, M. Vernon and W. Long, The effects of self-absorption and detection geometry on fluorescence intensity and decay lifetime, SPIE, 2005.
- 55 E. Madirov, D. Busko, F. A. Cardona, D. Hudry, S. V. Kuznetsov, V. A. Konyushkin, A. N. Nakladov, A. A. Alexandrov, I. A. Howard, B. S. Richards and A. Turshatov, Adv. Photonics Res., 2022, 2200187.
- 56 G. Gao, D. Busko, N. Katumo, R. Joseph, E. Madirov, A. Turshatov, I. A. Howard and B. S. Richards, Adv. Opt. Mater., 2021, 9, 2001901.
- 57 G. Ren, D. Shen, S. Wang and Z. Yin, J. Cryst. Growth, 2002, 243, 539-545.
- 58 M. Y. Hossan, A. Hor, Q. Luu, S. J. Smith, P. S. May and M. T. Berry, J. Phys. Chem. C, 2017, 121, 16592-16606.